

Tyre contact surface for the fatigue design of orthotropic steel bridge decks

Jorrit D. Rodenburg^a, Johan Maljaars^{a,b,*}, Sjoerd T. Hengeveld^{a,b}, Adri H.J.M. Vervuurt^a

^a Reliable Structures, TNO, Molengraaffsingel 8, Delft, 2629 JD, The Netherlands

^b Structural Engineering and Design, Eindhoven University of Technology, De Zaal 1, Eindhoven, 5612 AZ, The Netherlands

ARTICLE INFO

Keywords:

Fatigue
Traffic loads
Tyre contact surface
Orthotropic bridge deck

ABSTRACT

The fatigue life of orthotropic steel bridge decks in road bridges depends on the load effects exerted by heavy lorries. The contact surface of tyres is one of the important variables. Measurements described in the literature demonstrate that the actual tyre contact surfaces of today's traffic representative for Europe are shorter and slightly wider than the contact surface defined for the load model in the European standard for fatigue loads in bridges — EN 1991-2. This paper derives a new, realistic tyre contact surface to be used with the tyre loads in EN 1991-2, in such a way that the load effects for fatigue are realistically captured and that the required safety level is met.

1. Introduction

Structural fatigue of Orthotropic steel Bridge Decks (OBD) in motorway bridges caused by crossing axles of heavy vehicles is a concern of practical relevance [1–4]. The structural design of OBD is driven by fatigue. The load effect in many of the welded details depends not only on the axle load, but also on the load transfer through tyres, because these define the surface over which the load is distributed as well as the contact stress distribution over that surface. Fig. 1 provides the five fatigue sensitive welded details that are located directly below the deck plate and that are therefore most sensitive to the tyre contact surface and the contact stress distribution.

Following the standard EN 1991-2 [5], three types of axle are distinguished, namely, Type A for steering axles, Type B for double tyre (mainly traction) axles and Type C for wide base single tyre rear axles. Measurements are reported containing information on the tyre contact surface for each of these tyres. Nieuwsma [6] provides the most common types of tyre in Europe, see Fig. 2 for the tyre designation: Type A axles and Type B traction axles usually contain 315 / 80 R 22.5 tyres and type C axles usually contain 385 / 65 R 22.5 tyres. Type B non-traction axles usually contain 275 / 70 R 22.5 tyres but these are not so common in current traffic in continental Europe and they are further not considered. Table 1 provides important characteristics of the axle types. The second column of the table gives the tyre inflation pressures p_{ifl} as measured from a few hundred tyres (other columns will be introduced below). These are representative for European traffic; inflation pressures measured in the United States are slightly lower [12]. The stress distribution q is non-uniform over the gross width W_g and the length L of the contact surface. A distinction can be made between the

centre of the gross width, where the inflation pressure p_{ifl} determines to a large extent the maximum contact stress, and the outer parts of the gross width, where the tyre load F_{tyre} determines the maximum contact stress [8,10,13–15]. The contact stress is negligible at the tread grooves of new tyres and hence the load is transferred in between these tread grooves. Even in heavily worn tyres the contact stress at the tread grooves is lower than in between [16].

In length direction, the contact stress is best described with a trapezoidal [10,11] or semi-elliptical [8,14] shape, which can vary between the tread grooves [17]. The length of the contact surface L increases with the tyre load F_{tyre} and it decreases with the tyre inflation pressure p_{ifl} [8–10,18]. Contrarily, the gross width W_g appears almost independent of the tyre load and inflation pressure ranges of relevance [8,9]. The tyre contact surface has an almost rectangular shape for high tyre loads and it tends towards a circular shape for low tyre loads [8,9,11]. The inflation pressures and the tyre contact surfaces of Table 1 have been measured at very low vehicle speed or standstill. De Beer and Fisher [17] recommend to carry out measurements at full speed. However, Tielking and Roberts [19] conclude that the vehicle speed has almost no influence on the contact stress distribution.

The European standard for traffic loads on bridges EN 1991-2 [5] is used for the fatigue design of European bridges. Fatigue Load Model 4 (FLM4) of that standard is suited for the fatigue design of OBD. It consists of a set of five predefined lorries, each with a number of axles of type A, B or C with a certain axle load. For ease of use, EN 1991-2 [5] provides a simplified representation of the tyre contact surface and the stress distribution of the tyres of the three axle types, where the contact length L is a fixed value irrespective of the axle load and the inflation

* Corresponding author.

E-mail address: johan.maljaars@tno.nl (J. Maljaars).

Table 1
Axle description and characteristics according to FLM4 in [5] and literature.

Axle Type (description)	p_{ifl} ^a [kPa] [6,7]	W_g FLM4 [mm]	W_g [8,9] [mm]	F_{tyre} ^b FLM4 [kN]	L FLM4 [mm]	L^c [8–11] [mm]
A (steering)	700–900	220	225–260	35	320	250–320
B (double tyre, traction)	700–800	220	225–260	22.5	320	200–260
C (wide base single, rear)	800–900	270	270–310	37.5	320	250–320
				45	320	220–260

^aOutliers are excluded.

^bListed are the maximum and minimum tyre loads in FLM4. Allowance for dynamic amplification is included in the loads in FLM4.

^cThe tyre contact length is given that corresponds to F_{tyre} of FLM4.

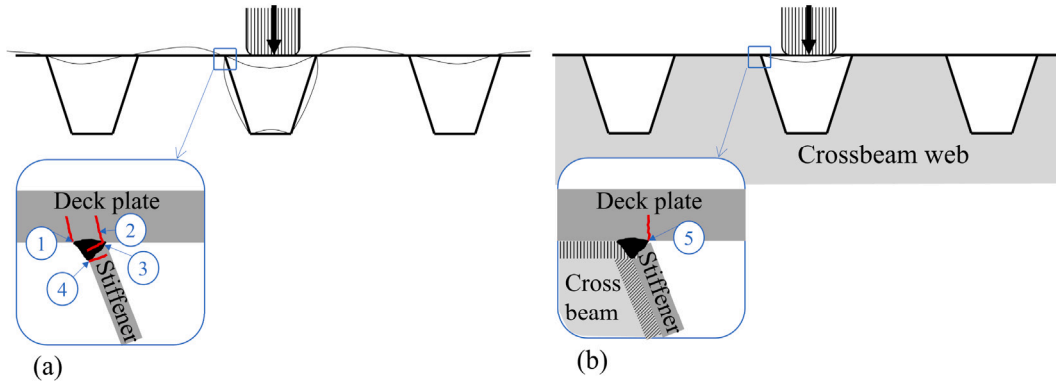


Fig. 1. Five details in OBD sensitive to the tyre contact surface: (a) Detail 1–4 in between crossbeams; (b) Detail 5 near the crossbeam intersection.

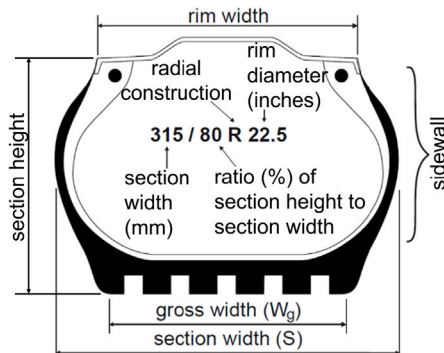


Fig. 2. Tyre designation.

pressure, and where a uniform stress distribution is applied over the contact surface without consideration of the tread grooves. Fig. 3(c) and (d) provide the stress distribution in the standard of a large and a small tyre load, whereas Fig. 3(a) and (b) give a schematic representation of realistic stress distributions of the same loads. According to the background document [20] of EN 1991-2, the tyre contact surface in the standard is based on Prat and Jacob [21], who assume that the tyre contact stress is equal to the inflation pressure. The contact length then follows from the difference in tyre radius between an unloaded and a loaded tyre. The stiffness of the tyre sidewalls is ignored in this approximation. To the authors' knowledge, the contact length according to [21] is not validated with tests. Columns 3 to 7 of Table 1 give a comparison of the tyre contact surfaces of FLM4 and the sources mentioned above. It appears that the contact surface widths in FLM4 are lower bound values and that the contact surface lengths in FLM4 are generally longer than measured. However, a direct evaluation of the contact surface between FLM4 and measurements cannot be made based on these data because of the different contact stress distribution and because FLM4 is intended to be conservative, thereby allowing

for dynamic amplification and load (effect) uncertainties and dynamic amplification. The AASHTO LRFD bridge design specifications [22] also use a uniformly distributed load over a rectangular surface, the latter prescribed as $L \cdot W_g = 254 \text{ mm} \cdot 254 \text{ mm}$ for steering axles and $254 \text{ mm} \cdot 518 \text{ mm}$ for two combined tyres of double tyre axles.

The purpose of this paper is to evaluate the contact surface in FLM4 and to derive a realistic tyre contact surface such, that the load effects of FLM4 provide the intended level of conservatism. The general ease of use of FLM4 is thereby preserved, i.e., a uniform contact stress and a fixed contact width and length. Finally, some additional modifications to FLM4 are proposed.

2. Methods

2.1. Outline

The study comprises four analyses as outlined in Fig. 4. The analyses are described briefly here and in more detail in the subsequent subsections. Analysis 1 intends to provide a fatigue damage evaluation based on a realistic representation of the tyres. Axle loads are obtained from a Weigh In Motion (WIM) database. Based on the literature sources mentioned in the introduction, a realistic contact surface and stress distribution is selected for each axle in the WIM database. The tyre contact surfaces with their contact stress are applied on a finite element model (FEM) of an OBD, from which the stress ranges in the welded detail of study are extracted. The lateral position of the tyre is randomly selected from a distribution. Employing the S–N curve of the detail, the theoretical fatigue damage is determined.

Analysis 2 consists of a modified version of FLM4, denoted as FLM4* to distinguish with the original FLM4 according to EN 1991-2. The axle loads are taken according to FLM4 and a uniform contact stress is applied on a tyre contact surface with a fixed length. The same FEM model and S–N curve as in Analysis 1 are employed to determine the damage. The damages of Analyses 1 and 2 can then be compared, but they are not necessarily equal because FLM4* is intended to be conservative. For this reason, Analysis 3 is added which is a combination of Analyses

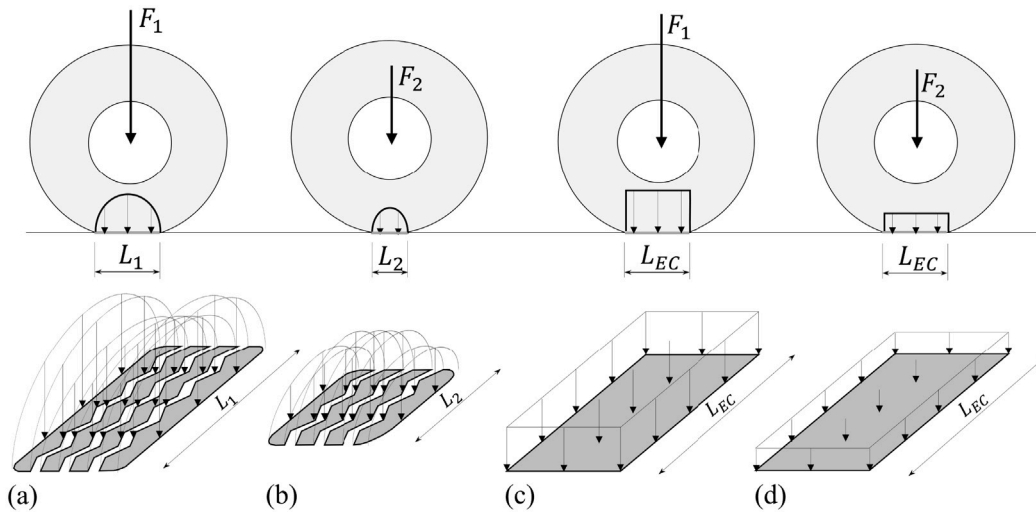


Fig. 3. Schematic of the tyre contact surface: (a) Realistic contact surface of a large tyre load F_1 ; (b) Realistic contact surface of a small tyre load F_2 ; (c) FLM4 contact surface of F_1 ; (d) FLM4 contact surface of F_2 .

1 and 2; the axle loads of the WIM database (Analysis 1) are used but the tyre contact surface and contact stress distribution are according to FLM4* (Analysis 2) in Analysis 3, thereby excluding the effect of the approximation of the tyre contact. It is assumed that the difference in fatigue damage between Analysis 2 and 3 provides the desired level of conservatism of the load model, because the load model should have the same level of conservatism for welded details sensitive to the tyre contact (Analysis 2 versus 1) and details insensitive to the tyre contact (Analysis 2 versus 3). Finally, Analysis 4 includes the uncertainties in the load effects and in the S–N curves with the aim of determining the reliability level in terms of the reliability index β , for a design according to FLM4* using stress ranges multiplied with partial safety factors γ_{Mf} and γ_{Ff} .

2.2. Welded detail of study and its S–N curve

A preliminary study into the sensitivity of the tyre contact surface is carried out on Details 3 and 5 of Fig. 1, see [23]. It was found that the theoretical fatigue verification of both details depends significantly on the tyre contact approximation. Detail 5 – which is the crack starting from the root of the weld between the stiffener and the deck plate, and growing into the deck plate, at the intersection with the crossbeam web – is selected for analysis in this study. Reason is that the influence surface of Detail 3 (as well as those of Details 1, 2 and 4, which are all located in the span between crossbeams) is longer than for Detail 5 so that, given the distances between axles, more than one axle load the influence surface simultaneously for Detail 3. This complicates the evaluation of the influence of the tyre contact. Detail 5 is loaded by individual axles, which makes this detail suited for a quantitative comparison of tyre contact surfaces. From a theoretical perspective, the choice of detail does not influence the results, because the same detail is used in all four analyses.

Constant amplitude fatigue test data of Detail 5 are given in [9,24–30]. The specimens in [30] had a 16 mm thick deck plate, but the stress range used is not defined. All other studies contained a relatively thin deck plate of 12 mm and reported the hot-spot stress range. The 12 mm test data are used to validate a fracture mechanics model [31] and this model is subsequently used to estimate the fatigue strength of thicker deck plates and to estimate the shape of the S–N curve in the long life region:

$$N = \begin{cases} \max [C_1(\Delta\sigma_{hs})^{-3}, C_2(\Delta\sigma_{hs})^{-5}] & \text{if } \Delta\sigma_{hs} > \left(\frac{C_2}{3 \cdot 10^8}\right)^{1/5} \\ \infty & \text{otherwise} \end{cases} \quad (1)$$

Table 2

Parameters of the S–N curve for 95% survival probability (units N, mm).

t	$\log_{10}(C_1)$	$\log_{10}(C_2)$
12	12.99	16.79
20	13.20	17.14

where N is the number of cycles to failure, $\Delta\sigma_{hs}$ is the hot-spot stress range, and parameters C_1 and C_2 are given in Table 2.

Fig. 5(b) provides the resulting hot-spot stress S–N curves with 95% survival probability of 12 mm and 20 mm thick deck plates, where the hot-spot stress range values given in the graph are the fatigue reference strengths at $N = 2 \cdot 10^6$ cycles. Explanations of the high fatigue strength are given in [31]. Despite this high fatigue strength, Detail 5 is often decisive in OBD because of the high hot-spot stress range caused by the applied load for this detail [32]. The estimated knee-points are in between the standardised S–N curve shapes of standards EN 1993-1-9 [33] and BS 7608 [34], Fig. 5(c).

The fatigue damage is determined with the linear accumulation rule of Palmgren [35] and Miner [36]. Since each crossing axle creates a single cycle for Detail 5:

$$D = \sum_{i=1}^{n_{ax}} \frac{1}{N_i} \quad (2)$$

where n_{ax} is the number of crossing axles during the life.

2.3. Design load model FLM4*

FLM4* used in Analysis 2 consists of five predefined vehicles with characteristics according to Table 3. The fractions per vehicle of the total number of vehicles n_{obs} in the table are given for long-distance traffic, with n_{obs} specified as $2 \cdot 10^6$ per year per slow lane. The original FLM4 in [5] is based on WIM data from the 1980's [20], but the load effects appear still conservative compared to today's traffic for influence lengths shorter than 20 m [37]. However, axle Type B for non-traction rear axles was relatively common in those years, whereas these are gradually replaced by axle Type C since that time and this trend is expected to continue in future. Another observed trend is that Vehicle 3 lorries operate with one or two rear axles lifted in case light-weight freight. For this reason the rear axles of Vehicle 4, which are of axle Type B in FLM4, are changed to axle Type C in FLM4* and the fractions of Vehicles 3 and 4 are altered, both changes in agreement with the Dutch National Annex to [5].

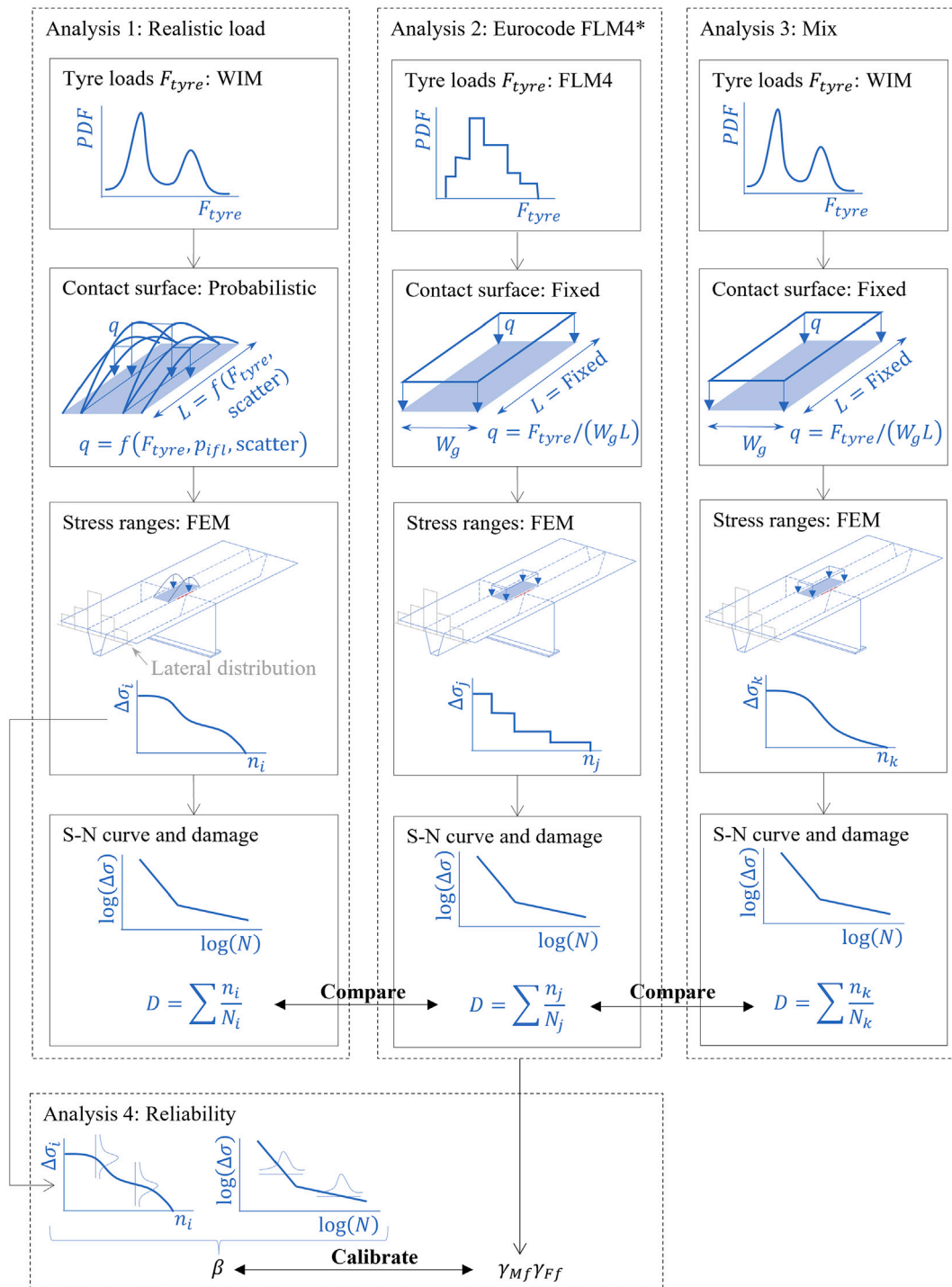


Fig. 4. Outline of the analyses in this paper.

Table 3
Vehicles comprising FLM4*.

Vehicle	Number of axles	Axle types	Axle loads [kN]	Axle distances [m]	Fraction of n_{obs}
1	2	A B	70 130	4.5	0.20
2	3	A B B	70 120 120	4.2 1.3	0.05
3	5	A B C C C	70 150 90 90 90	3.2 5.2 1.3 1.3	0.40 ^b
4	4	A B C ^a C ^a	70 140 90 90	3.4 6 1.8	0.25 ^b
5	5	A B C C C	70 130 90 80 80	4.8 3.6 4.4 1.3	0.10

^aThese axles are defined as axle Type B in FLM4.

^bFraction of Vehicle 3 is 0.50 and that of Vehicle 4 is 0.15 in FLM4.

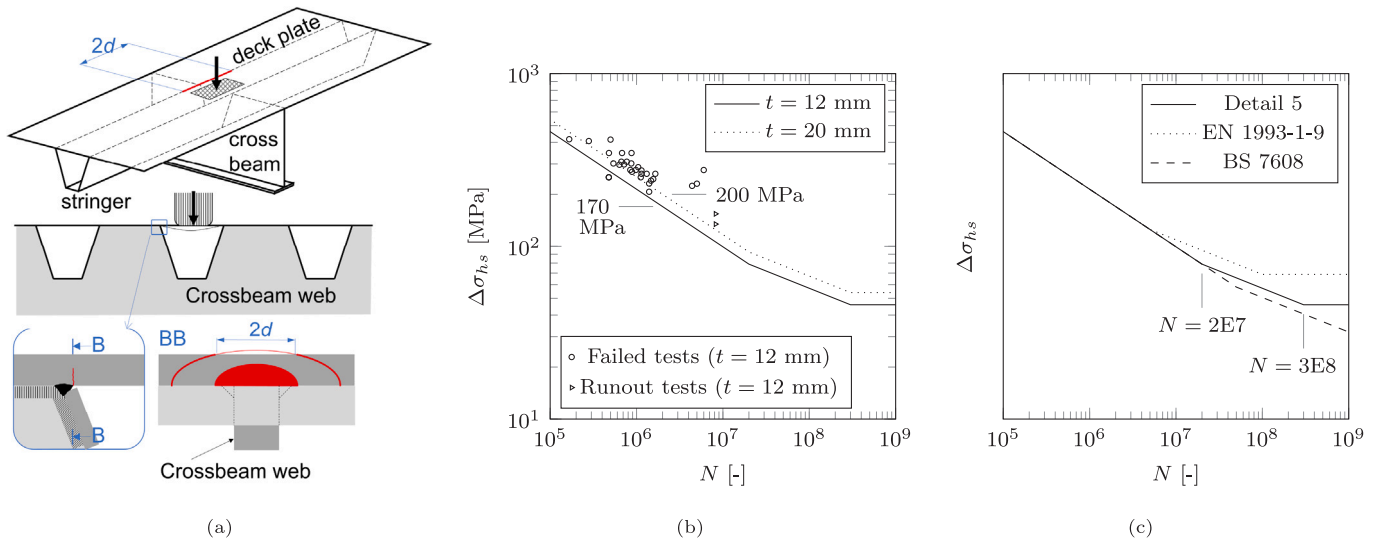


Fig. 5. Fatigue of Detail 5: (a) Typical crack location; (b) S–N curves; (c) Shape of variable amplitude S–N curve compared to standards.

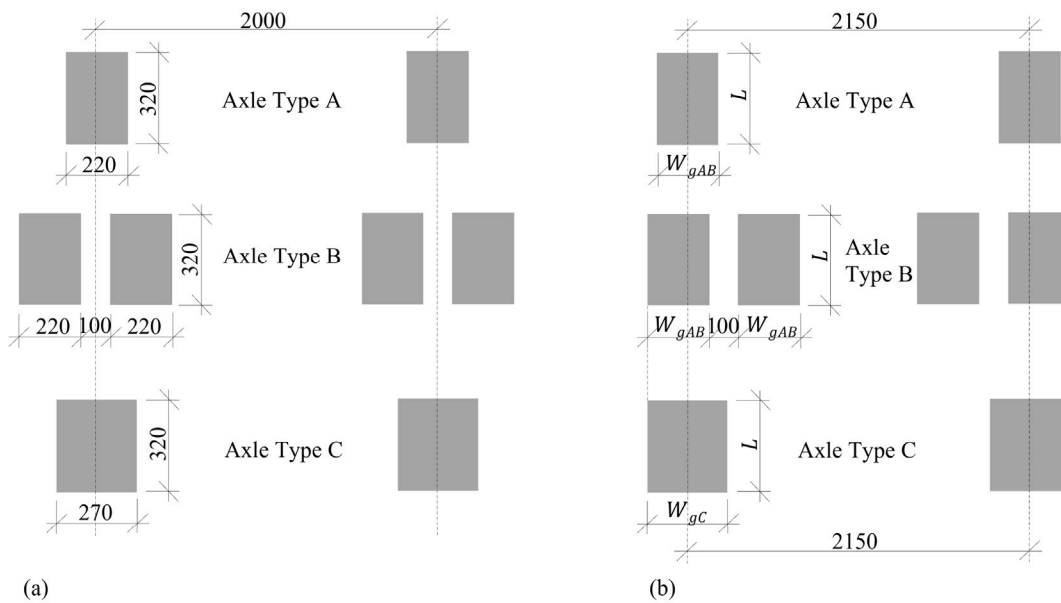


Fig. 6. Axles lay-out (dimensions in mm): (a) in FLM4; (b) in FLM4*.

Fig. 6(a) gives the lay-out of the axles and the corresponding tyre contact surfaces in FLM4. A few modifications are applied in FLM4*, Fig. 6(b):

- The exterior width of axle Type B in FLM4 is larger than that of axle Type C. Data of vehicle manufacturers and measurements indicate that the exteriors of axle Types B and C are approximately equal (the exterior width of axle Type A is smaller to accommodate steering). This is changed in FLM4*, in agreement with [38].
- Table 1 shows that the tyre contact widths in FLM4 are the lower bounds of measurement data. Two sets of simulation are applied, namely, with tyre contact widths according to FLM4 and with average tyre widths according to measurements. The latter set has a tyre contact width of $W_{gAB} = 235$ mm for axle Types A and B and $W_{gC} = 290$ mm for axle Type C.
- The tyre contact length L is calibrated with the procedure outlined in Section 2.1 for each set of tyre contact width. Similar to FLM4, the value of L is equal for all axles and axle types. The

uniform contact stress follows from Eq. (3).

$$q = \frac{F_{ax}}{n_{tyre} W_g L} \quad (3)$$

where F_{ax} is the axle load (Table 3) and n_{tyre} is the number of tyres per axle.

The position of vehicles in lateral direction is subject to variation. Fig. 7 gives the frequency distribution of the transverse location of the vehicle centre in FLM4, which is also used in FLM4*.

2.4. Representation of the realistic load

The axle loads used for the realistic load representation in Analysis 1 are taken from a WIM database in Motorway A16, The Netherlands. This database is described, validated and compared to other WIM databases from European motorways in [39,40]. It appears from [39] that the axle loads have not significantly changed in the years between 2008 and 2018, and the database used here dates from April 2008.

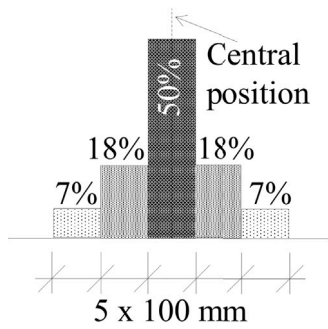


Fig. 7. Frequency distribution of the transverse vehicle location in FLM4.

This database contains 207,000 vehicles and 903,000 axles driving on the slow lane. The WIM database does not provide the type of axle. The axle types are therefore based on the automatic vehicle categorisation and the corresponding typical axle types following from vehicle manufacturers and expert judgement. Fig. 8 gives the axle loads in the WIM database per axle type. The weight spectrum of the steering axle is close to narrow-banded and those of axle Types B and C are multi-modal. Note that the WIM database does not contain dynamic amplification due to vehicle-structure interaction. The latter appears small, see Appendix, and it is considered in Analysis 4.

A number of approximations are put forward in the realistic representation of the tyre contact surface and the contact stress in Analysis 1:

- A study of pultruded fibre reinforced decks showed that the load effect of the actual tyre contact surface can be well approximated with a rectangular surface, in particular for somewhat higher tyre loads relevant to fatigue [41]. It is expected that this conclusion also holds for details in OBD and therefore a rectangular contact surface is used.
- The difference in contact stress at the tyre tread grooves and in between will not affect the stresses in details in the OBD because the stress is transferred through the deck plate. The stress is averaged over the grooves and in between grooves for this reason.
- Following [10,13,14], the tyre contact width is divided into three zones, namely, the two outer zones each comprising 20% of the gross width W_g and the centre comprising 60% of W_g . The contact stress is constant in width direction in each of these zones, with maxima over the length denoted as q_{out} and q_{cen} , respectively.
- The contact stress in length direction follows a semi-elliptical shape.

Fig. 9 gives a schematic representation of the approximation of the tyre contact surface and contact stress. The equations fitted to measurements in [10] are used for the ratio r_q between the maximum contact stress in the outer zones and the centre zone:

$$r_q = \frac{q_{out}}{q_{cen}} = \frac{\left(85.5 + 9.25 \frac{F_{tyre}}{[kN]} + 0.290 \frac{p_{ifl}}{[kPa]}\right) [MPa]}{c \left(422 - 1.2 \frac{F_{tyre}}{[kN]} + 0.00461 \frac{F_{tyre}}{[kN]} \frac{p_{ifl}}{[kPa]} + 0.322 \frac{p_{ifl}}{[kPa]}\right) [MPa]} \quad (4)$$

where c accounts for the fact that tread grooves are not present in the outer zones of axle Type C tyres (factor not given in [10], but derived here based on ink prints in [9]; data in [10] are the maximum values between the grooves). Factor c is determined as 0.7 in for axle Type C tyres and it is equal to unity for axle Type A and B tyres. Following the findings in [19], see Section 1, the effect of vehicle speed in the original equations of Groenendijk [10] has been ignored in Eq. (4). Based on the sources in Section 1, the tyre inflation pressures p_{ifl} are distributed with a mean equal to 8.6 bar, 8.3 bar and 8.6 bar for axle Types A, B

and C, respectively, and their standard deviations are 0.82 bar, 0.82 bar and 0.65 bar, respectively. A value of p_{ifl} is randomly selected from these distributions for each tyre load F_{tyre} in the WIM database and the ratio r_q is determined from Eq. (4).

It is concluded in Section 1 that the tyre contact width is largely independent of p_{ifl} and F_{tyre} . The average of the gross widths of the measured tyre contact is used ($W_g = 235$ mm for tyres of axle Types A and B, and $W_g = 290$ mm for tyres of axle Type C).

The tyre contact length L depends on p_{ifl} and F_{tyre} (Section 1). However, the number of measurement data is too small to establish a reliable relationship between the three variables. The scatter in inflation pressure between tyres is relatively small, Table 1. Therefore, L is selected as dependent on F_{tyre} based on the available measurements with their mean and standard deviation, where the standard deviation describes the lumped uncertainty, including the effect of the variation of p_{ifl} . Fig. 10 gives the measured data in terms of tyre contact length versus tyre load for $F_{tyre} \geq 15$ kN and $6 \leq p_{ifl} \leq 10$ bar. Note that the data from [8] in Fig. 10(a) are for tyre type 11 R 24.5, but this type is similar to 315 / 80 R 22.5, and the data from [10] in Fig. 10(b) are for tyre type 425 / 65 R 22.5, but this type is similar to 385 / 65 R 22.5. The relationship between tyre load and tyre length is described with a mean m_L and a coefficient of variation V_L . In Analysis 1, the tyre contact length for each tyre load in the WIM database is randomly selected from a normal distribution with m_L and V_L :

$$m_L = 2.81 F_{tyre} [\text{mm/kN}] + 169 [\text{mm}]; V_L = 0.081 \text{ for axle Types A and B} \quad (5)$$

$$m_L = 2.45 F_{tyre} [\text{mm/kN}] + 130 [\text{mm}]; V_L = 0.062 \text{ for axle Type C} \quad (6)$$

For reference, Fig. 10 also provides the linear regression curves and the lengths and tyre loads used in FLM4.

Finally, it is assumed that the axle load is equally divided over the tyres of that axle. The maximum values of the contact stress of each tyre, q_{cen} and q_{out} , then follow from equilibrium and from the ratio r_q in Eq. (4):

$$F_{ax} = n_{tyre} \left(0.6 W_g q_{cen} + 2 \cdot 0.2 W_g r_q q_{cen}\right) \int_{-0.5L}^{0.5L} \sqrt{1 - (2x/L)^2} dx \quad (7)$$

$$q_{out} = r_q q_{cen} \quad (8)$$

The distances between the tyres of an axle are taken equal to those of FLM4*, Fig. 6(b).

For traffic lanes with usual width – approximately 3.3 to 3.5 m – the standard deviation of the lateral vehicle position of current traffic appears larger than EN 1991-2 [5] suggests, [32]. However, automatic vehicle driving may imply a reduction in the standard deviation compared to current traffic in future. The distribution of [5], Fig. 7, is therefore used in Analysis 1. A lateral position is selected from this distribution per vehicle, so that all axles of that vehicle have the same lateral position.

2.5. Finite element model

The importance of the tyre contact surface is larger for OBD with thin pavement as compared to thick pavement, because the pavement causes dispersion of the load. The pavement on movable bridges is often very thin – e.g., an epoxy layer of a few millimeters thick – and the load dispersion through such a layer is negligible. To compensate for the lack of pavement, the deck plate needs to be relatively thick. An OBD without pavement is considered in the analyses with a deck plate thickness of $t = 20$ mm, the latter based on the design of various movable bridges in The Netherlands. Fig. 11 provides the geometry of the OBD considered.

The OBD is modelled in the finite element software Abaqus 2020 using solid elements. The geometry consists of five stiffeners and three

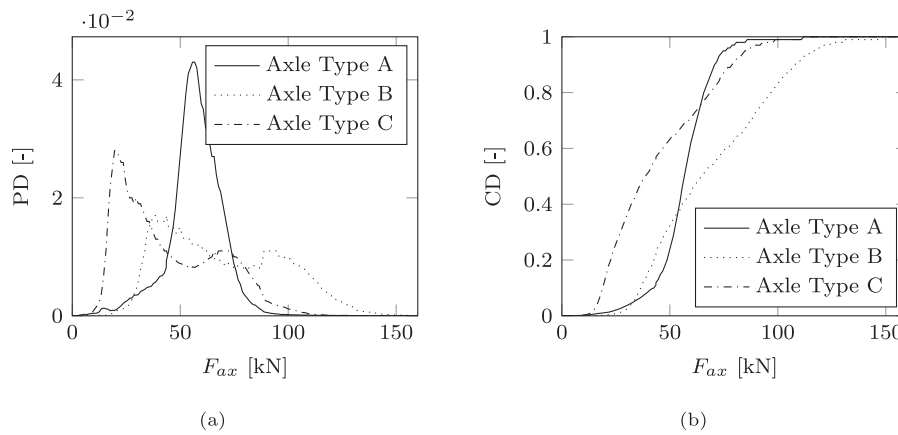


Fig. 8. Axle load distribution of the WIM database from motorway A16, The Netherlands: (a) Probability Density (PD) plot; (c) Cumulative Distribution (CD) plot.

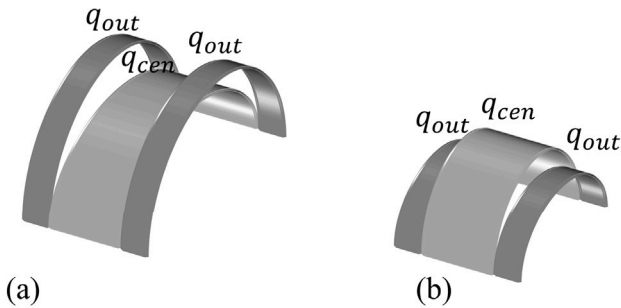


Fig. 9. Approximation of the realistic tyre contact surface and contact stress: (a) For relatively small loads; (b) For relatively large loads.

crossbeams, but symmetry in the longitudinal direction (x) is made use of, see Fig. 12. The crossbeams are supported in vertical (y) direction along their length at the intersection between the bottom flange and the web. The following welds are modelled explicitly: between crossbeam and deck plate, between crossbeam and stiffener and between stiffener and deck plate, the latter including the lack of penetration of 1.5 mm (Fig. 11). The hot-spot stress is determined with linear extrapolation to the weld root from the stresses in transverse (z) direction at distances of $0.5t$ and $1.5t$ from the weld root, similar to the hot-spot stress definitions in [9,25,27,31]. Linear elastic material is modelled with a Youngs modulus of 210 GPa and a Poisson ratio of 0.3. The grey volume in the right top graph of Fig. 12 is constructed with second order hexagonal elements with reduced integration, type C3D20R. These elements are suited for nodal stress extraction required for the hot-spot stress. The remainder of the geometry (displayed in blue) is modelled with linear hexagonal elements of type C3D8. These elements are used for easy application of nodal forces. The deck plate contains at least two elements in thickness to prevent mesh locking. A multi-part mesh refinement is used, explained and verified for Detail 5 in [31]. Tie constraints are used to transfer displacements between the parts with different mesh size.

The elements faces on the deck plate surface are of unequal size. A Python script is developed that uses the lateral vehicle position, axle load, axle type, tyre contact length, tyre contact width and contact stress distribution as input data and that distributes the contact stress to nodal forces applied on the nodes of at deck plate surface in the FEM using linear superposition. Subsequently it determines the hot-spot stress for Detail 5.

2.6. Reliability estimate

Structures should meet a certain legislative or standardised structural reliability. In practical assessments, this is achieved by multiplying all axle loads in FLM4* with a partial safety factor γ_{Ff} and dividing the resistance expressed through stress range in the characteristic S-N curve by a partial safety factor γ_{Mf} . The relationship between the structural reliability and the required partial factors is established in Analysis 4 (see Fig. 4) using two steps. Step 1 is the probabilistic assessment. It uses the hot-spot stress ranges determined in Analysis 1 – using the realistic tyre contact representation – multiplied with the following multiplicative uncertainty factors: M_{glob} for the uncertainty in estimating the global force transfer due to approximations applied in the engineering model, M_{scf} for the uncertainty in the hot-spot stress concentration factor estimation, M_{dyn} for the dynamic amplification, M_{wim} for the uncertainty in the axle load measurements, and M_{tr} for future changes (trends) in average axle load. Appendix of this paper estimates the distributions of these factors. The factors M_{dyn} , M_{wim} and M_{tr} cause a change in the tyre contact surface. It is unfeasible to apply the Python script for determining the stress range of each axle in each probabilistic computation because of the large computation time involved. For this reason, the effect of the changing tyre contact surface is estimated from the non-linear force–stress relationship of all computations of Analysis 1. The tangent τ_σ of the mean of that relationship is used as an approximation of the probabilistic hot-spot stress range $\Delta\sigma_p$, see Fig. 13:

$$\Delta\sigma_p = \Delta\sigma_{hs} M_{glob} M_{scf} \left(1 + \frac{\tau_\sigma}{\tau_0} [M_{dyn} M_{wim} M_{tr} - 1] \right) \quad (9)$$

where τ_0 is the secant of the relationship, describing a proportional increase in the hot-spot stress with tyre load.

Step 1 also uses a probabilistic S–N curve with the format according to Eq. (1), but with $\Delta\sigma_{hs}$ replaced by $\Delta\sigma_p$ and with C_1 and C_2 replaced by their probabilistic counterparts C_{1p} and C_{2p} , respectively. The distribution of C_{1p} is determined from the fatigue tests in [9,25,27], see Fig. 5(b): a lognormal distribution with a standard deviation of $\log_{10}(C_{1p}) = 0.175$ and a mean of $\log_{10} C_{1p} = C_1 + 1.645 * 0.175$. Variable C_{2p} is fully correlated to C_{1p} . The limit state function g is:

$$g = D_{cr} - D \quad (10)$$

where D_{cr} is the damage at failure. Based on the proposal in [42], the JCSS probabilistic model code [43] recommends a lognormal distribution for D_{cr} with a mean of 1 and a standard deviation of 0.3.

Table 4 provides the distributions of the random variables X .

The failure probability $P_f(X)$ is estimated from a Monte Carlo simulation. The reliability index β – referring to the entire life – is as follows related to the failure probability $P_f(X)$:

$$\beta = -\Phi^{-1}[(1 - P_{d|f})P_f(X)] \quad (11)$$

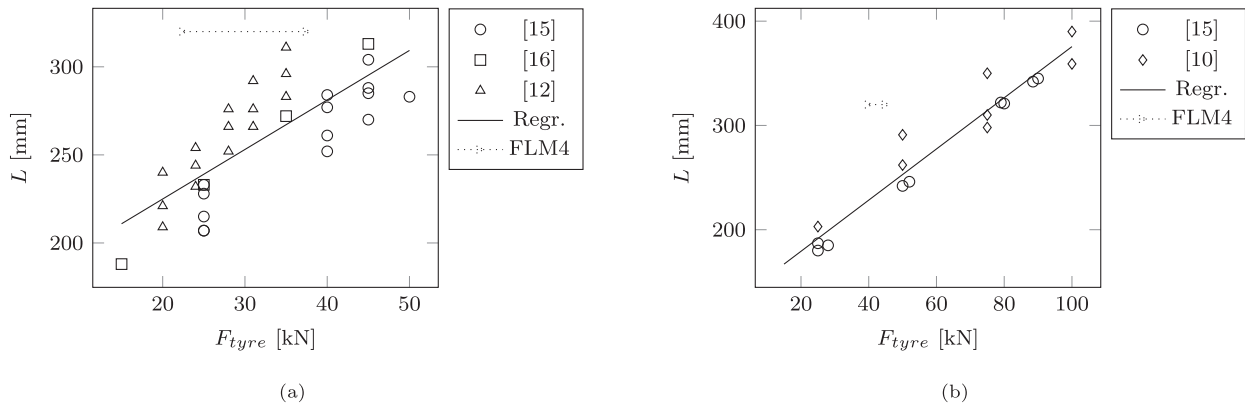


Fig. 10. Dependency of the tyre contact length L on the tyre load F_{tyre} : (a) For tyres 315 / 80 R 22.5 or 11 R 24.5 (steering axles and double tyre traction axles, types A and B); (b) For tyres 385 / 65 R 22.5 (wide base singles, type C).

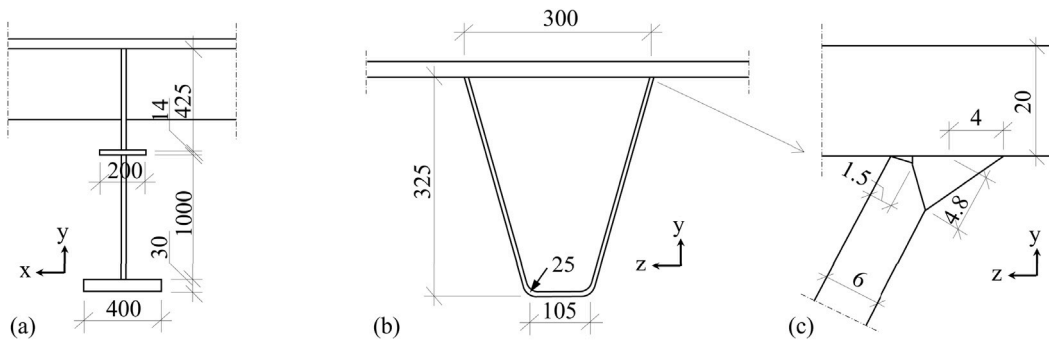


Fig. 11. Geometry of the modelled OBD: (a) Crossbeam; (b) Stiffener; (c) Deck plate (dimensions in mm).

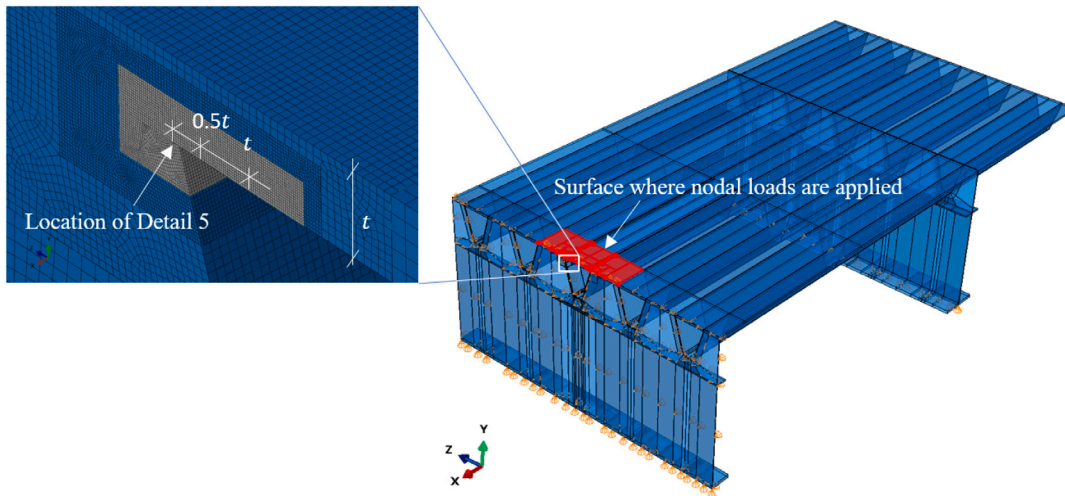


Fig. 12. Finite element model of the OBD with Detail 5 highlighted.

where Φ^{-1} is the inverse of the cumulative distribution function of the standard normal distribution and $P_{d|f}$ is the conditional probability that, given a crack has occurred, it is detected at a size at which: (1) it is still repairable without major disruption and; (2) it does not yet cause traffic accidents. The value is $P_{d|f} = 0$ by definition for a design without inspections and it is taken as $P_{d|f} = 0.8$ for a visually inspected OBD based on the estimate in [40] that 80% of fatigue cracks are detected in time.

Step 2 is the design check. The stress ranges of Analysis 2 – using FLM4* – are multiplied with partial safety factors γ_{Mf} and γ_{Ff} . The former factor is taken from prEN 1993-1-9 [44] and derived in [40],

see Table 5. Depending on the importance of the bridge, OBD are usually classified as giving small or medium failure consequences. The table also provides the target reliability indexes β_t for which the partial factors are derived. In Step 2, the partial factor γ_{Ff} is calibrated such that β of Step 1 correspond with the target β_t .

It is noted that γ_{Ff} in prEN 1990 [45] is determined using a probabilistic S–N curve of different shape than the one used here, namely, a Random Fatigue Limit (RFL) S–N curve which has a higher likelihood to fatigue test results [40]. The use of the random fatigue limit S–N curve results in a lower required partial factor γ_{Ff} [40]. The RFL S–N curve parameters require constant and variable amplitude

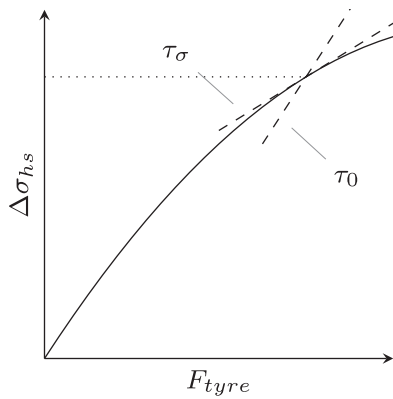


Fig. 13. Schematic representation of tangents τ of the tyre load versus hot-spot stress relation.

Table 4
Distributions of the random variables X (units: N, mm).

Symbol	Value or distribution ^a	Source
$\log_{10}(C_{1p})^b$	$\mathcal{N}(C_1 + 0.29, 0.18)$	this section
$\log_{10}(C_{2p})^{b,c}$	$\mathcal{N}(C_2 + 0.29, 0.18)$	this section
D_{cr}	$\mathcal{L}(1, 0.3)$	[43]
M_{glob}	$\mathcal{L}(1, 0.10)$	[43]
$\ln(M_{scf})$	$\mathcal{T}(0, 0.06, 6)$	Appendix
M_{dyn}	$\mathcal{L}(1, 0.02)$	Appendix
M_{lim}	$\mathcal{N}(1, 0.03)$	Appendix
M_{tr}	$\mathcal{N}(1.1, 0.005)$	Appendix

^a $\mathcal{N}(\cdot, \cdot)$ = normal distribution, $\mathcal{L}(\cdot, \cdot)$ = lognormal distribution, $\mathcal{T}(\cdot, \cdot, \cdot)$ = Student's t distribution. First position = mean, second position = standard deviation, third position = degrees of freedom.

^bSee Table 2 for C_1 and C_2 .

^cVariable C_{2p} is fully correlated to C_{1p} .

Table 5
Partial safety factors for the fatigue resistance γ_{Mf} in prEN 1993-1-9 [44] and target reliabilities β_i for which they are derived in [40].

Consequences of failure	Small	Medium	Large
	$\beta_i = 3.2$	$\beta_i = 3.7$	$\beta_i = 4.2$
Safe life design (no inspections)	1.1	1.25	1.35
Damage tolerant design (visual inspections)	1.0	1.15	1.25

test data with failures and run-outs at very high numbers of cycle. Such data are not available for Detail 5, nor for Details 1–4. As a comparison, the analyses of Steps 1 and 2 are repeated with a design S–N curve and a probabilistic RFL S–N curve of a cover plate detail, for which a relatively complete dataset is available (variables in [40]). Because the S–N curves in Steps 1 and 2 are based on the same data, the calibration of γ_{Ff} is considered realistic under the condition that the difference between the probabilistic S–N curve and the design S–N curve is independent of the type of weld detail.

3. Results and discussion

Fig. 14 presents the influence field determined according to Section 2.5, expressed as the hot-spot stress in Detail 5 $\Delta\sigma_{hs}$ for a unit contact stress on the deck plate q . Note that symmetry is used so 50% of the influence field is displayed. As expected, the hot-spot stress is almost zero for loads applied away from the stiffener of study and a negative hot-spot stress results for loads applied above the stiffener. However, a positive stress is obtained for loads applied very close to Detail 5. A closer examination shows that the element closest to Detail 5 experiences a negative stress for that load, but the extrapolation required for the hot-spot stress gives a positive stress.

Three central positions of the lateral vehicle distribution (Fig. 7) are considered, namely, with the tyres of axle Types A and C centred

Table 6
Average and equivalent tyre contact lengths in Analysis 1.

L_{av}	$L_{av50\%}$	L_{eq}
209 mm	251 mm	245 mm

above the stiffener, in between the stiffeners, or above the stiffener web, see Fig. 15(a). The former location (displayed in solid black) gives the highest fatigue damage and the results presented hereafter apply to this position. Fig. 15(b) gives the relative fatigue damage D_{bin} in bins of axle type and lateral position of Analysis 1 – using the realistic tyre contact representation – relative to the total damage D . The central lateral position is responsible for almost all damage. Further, axle Type A gives the largest damage contribution even though the number of axles is smaller than that of the other axles and the distribution tail with heavy axles is smaller than that of the other axles (Fig. 8). Axle Type B gives the smallest damage contribution whereas the average axle load is larger than that of the other types. This demonstrates the importance of the summed tyre contact surface per axle, which is relatively small for axle Type A and relatively large for axle Type B. Fig. 15(c) provides the hot-spot stress range as a function of the axle load of all vehicles in the central lateral position. The figure shows the expected non-linear relationship caused by an increasing tyre contact surface for an increasing axle load. The scatter in the figure demonstrates the influence of the variability in tyre contact length and tyre inflation pressure.

Table 6 gives the average contact length L_{av} of all axles in Analysis 1, the average contact length of the group of heavy axles causing 50% of the fatigue damage $L_{av50\%}$, and a damage equivalent contact length L_{eq} defined as:

$$L_{eq} = \frac{\sum_{i=1}^{n_{ax}} L_i D_i}{\sum_{i=1}^{n_{ax}} D_i} \quad (12)$$

All length values are considerably smaller than the length of 320 mm in FLM4.

Fig. 16 presents results of Analysis 2 – using FLM4* loads and tyre contacts definitions. Fig. 16(a) gives the relationship between the tyre contact length L and the relative fatigue damage for the two considered gross tyre widths: W_g according to FLM4 and according to the average of measurements. The fatigue damage is given for a design life of 100 years. The figure shows a significant influence of L on D . The discontinuity in the curve is caused by the cut-off value in the S–N curve at $N = 3 \cdot 10^8$ cycles in Fig. 5. This discontinuity is more significant in FLM4* than in the realistic tyre contact simulations, because of the step-wise axle load histogram in FLM4* with large numbers of axles having equal axle loads. The cut-off causes such a group of axles to either contribute to the fatigue damage or not contribute to it. There is no proof of the existence of a cut-off value [46,47]. For these reasons, Fig. 16(b) presents the results of the analysis without a cut-off, replacing Eq. (1) with:

$$N = \max [C_1(\Delta\sigma_{hs})^{-3}, C_2(\Delta\sigma_{hs})^{-5}] \quad (13)$$

This curve shows a continuous relationship that can be used for further analysis.

The damage comparison between Analyses 2 and 3, with the difference being the axle loads, is carried out for a tyre contact length $L = 320$ mm (the length of FLM4) and for $L = 220$ mm (an approximate lower bound of Fig. 10 and Table 6) and for lower bound tyre contact widths (the width of FLM4; $W_{gAB} = 220$ mm and $W_{gC} = 270$ mm) and average gross tyre widths ($W_{gAB} = 235$ mm and $W_{gC} = 290$ mm). The damage of Analysis 2 was 3.35 times larger than that of Analysis 3 for lower bound tyre contact widths and 3.19 times higher for average tyre contact widths, independent of the tyre contact length. As explained in Section 2.1, these damage ratios are considered as the intended

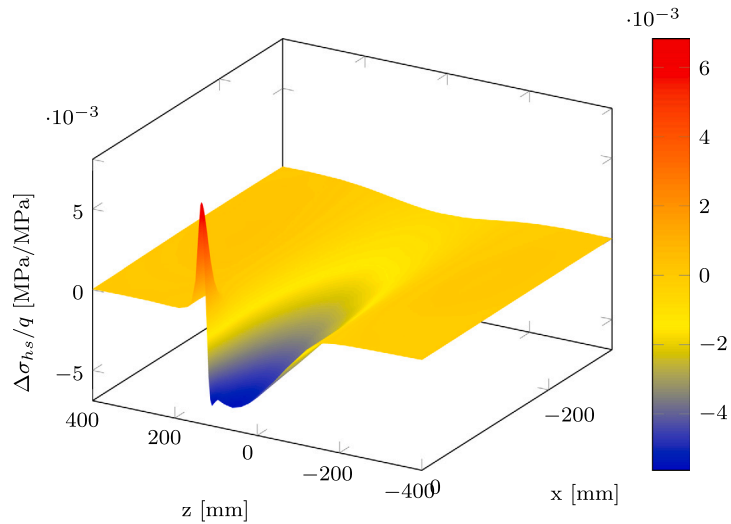


Fig. 14. Hot-spot stress influence field Detail 5 for a unit contact stress determined with the finite element model.

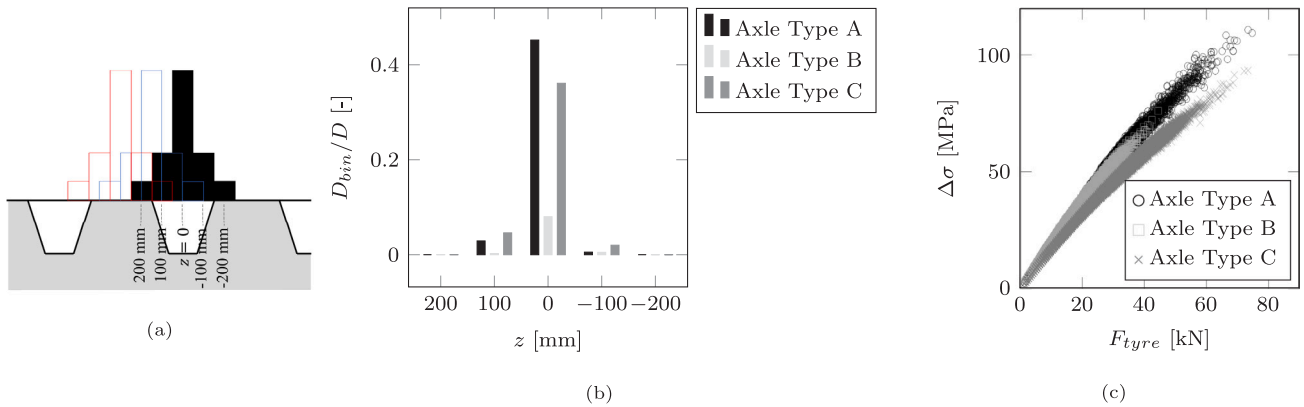


Fig. 15. Results of Analysis 1 – realistic tyre contact representation: (a) Lateral positions considered of axle Types A and C, with in solid black the positions of maximum damage; (b) Damage contribution per axle type and lateral position; (c) Stress range as a function of tyre load for the central lateral position.

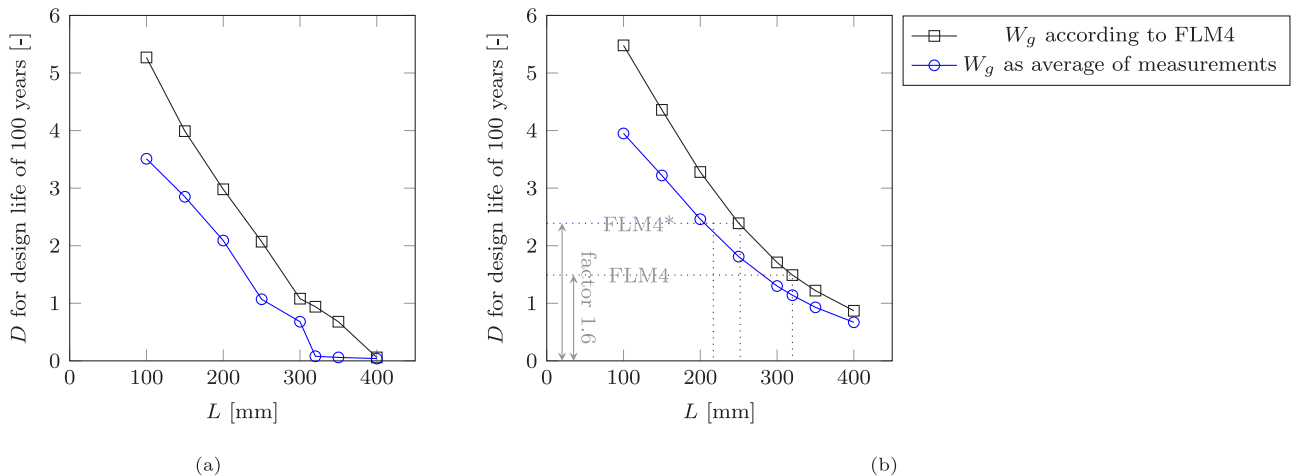


Fig. 16. Results of Analysis 2 – FLM4*: (a) Using the S–N curve of Fig. 5; (b) Using an S–N curve without cut-off.

implicit conservatism in FLM4. Subsequently, the tyre contact length L in Analysis 2 (FLM4*) is calibrated such that the damage is 3.35 or 3.19 times higher than that of Analysis 1 (realistic representation). This results in an FLM4* tyre length of $L = 252$ mm for the lower bound tyre contact widths and $L = 217$ mm for the average tyre contact widths. Both lengths are significantly smaller than the current FLM4

length of $L = 320$ mm. The conclusion is that the FLM4 tyre contact length is too large and it is therefore unconservative. For the geometry of Fig. 11, the damage using the FLM4 tyre contact length is a factor of 1.6 below target (Fig. 16). This conclusion is based on analysing Detail 5. Other details have a different influence field and hence a different dependency on the tyre contact length and contact width. The

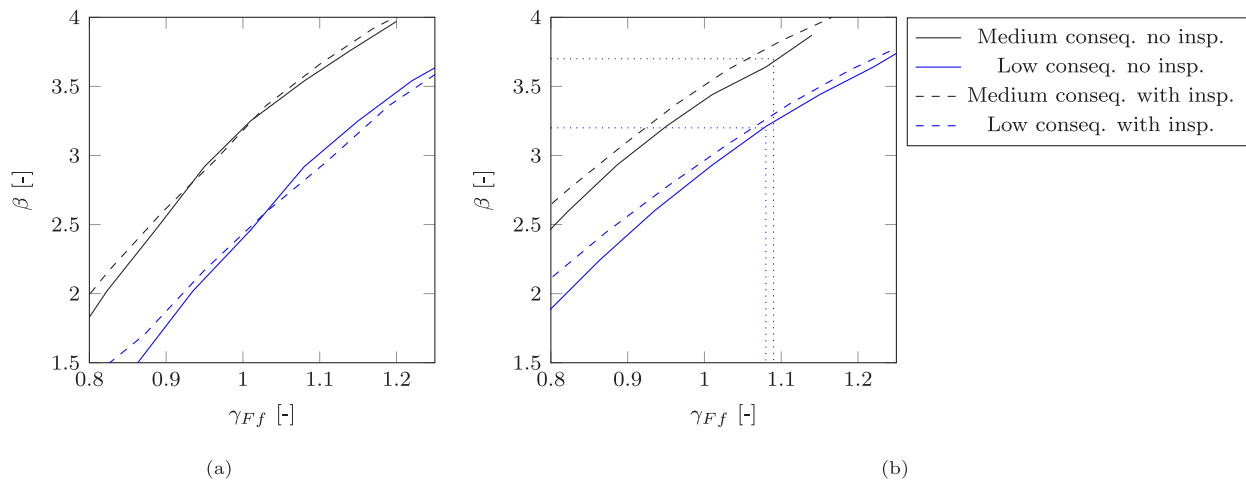


Fig. 17. Results of Analysis 4 – probabilistic – with the relationship of the partial factor on the load side γ_{Ff} and the reliability index β : (a) For the S–N curve format of Fig. 5; (b) For the RFL S–N curve.

calibrated contact surfaces are deemed valid for other details as well because the same influence field is applied in all four analyses.

Analysis 4 – the probabilistic analysis – is conducted to further verify the calibrated contact surfaces. The tangent τ_σ in Eq. (9) is determined from a polynomial regression curve of the data in Fig. 15(c). Fig. 17(a) presents the relationship between the partial factor γ_{Ff} and the reliability index β . The relationship is established for the new tyre contact surfaces of FLM4*. Note that the partial safety factors of the fatigue resistance γ_{Mf} of Table 5 are already included in the analysis. Fig. 17(b) gives a similar curve based on the RFL S–N curve. The required partial safety factor, indicated with the dotted lines, is approximately $\gamma_{Ff} = 1.1$ for this model. This value is equal to the value derived in [40] using the same RFL model and WIM database for influence lines of various length (between 1 and 200 m) that are not depending on the tyre contact surface. This supports the newly calibrated tyre contact surfaces of FLM4*.

4. Conclusions

This paper compares the simplified tyre contact surface of Eurocode's Fatigue Load Model 4 (FLM4 of EN 1991-2) with the tyre contact surface and contact stress distribution representing realistic conditions for application in orthotropic bridge decks. The tyre contact surface is calibrated such that it gives the desired level of conservatism in terms of fatigue damage and safety level. The following conclusions apply:

- The tyre contact length is a function of the tyre load and the tyre inflation pressure. The contact stress in length direction can be approximated as of trapezoidal or semi-elliptical shape (the latter is used in the current study).
- The tyre contact width is relatively constant, i.e., independent of tyre load and tyre inflation pressure. The exterior parts of the width carry a different fraction of the load than the central part of the width. The load fraction carried by the exterior parts increases with tyre load and it decreases with inflation pressure.
- The fatigue performance of deck plates in orthotropic bridge decks depends on the tyre contact surface and the tyre contact stress distribution. Steering axles, especially heavy ones, are smaller in number than other axle types, yet they are responsible for a relatively large damage contribution because of the small tyre contact surface. The opposite is true for double tyre traction axles: the average axle load is larger but the damage contribution is smaller than that of the other axle types because of the large summed tyre contact surfaces.

- For ease of use, FLM4 in the Eurocodes uses a constant tyre contact stress, a single tyre contact width for all axles of the same type, and a single tyre contact length for all axles. The tyre contact widths appear equal to the lower bounds of measured gross tyre widths.
- The tyre contact length of 320 mm in FLM4 appears too large for a consistent structural reliability. The level of conservatism of the load model is lower for details sensitive to the tyre contact surface than for details not sensitive to it. The required tyre contact length is calibrated as 252 mm for the lower bound contact width applied in FLM4 and as 217 mm for the average contact width. For these contact surface dimensions, the required safety level is the same as for other details not sensitive to the tyre contact surface.
- Other proposed improvements of FLM4 to better align with actual traffic data are a reduction of the exterior width of double tyre axles and a replacement of non-traction axles with four tyres by axles with wide base single tyres.

Declaration of competing interest

The authors declare that they have no known competing financial interests or personal relationships that could have appeared to influence the work reported in this paper.

Data availability

Data will be made available on request.

Acknowledgements

Rijkswaterstaat and Province Noord Holland are acknowledged for their financial contribution for carrying out the research. Frank van Dooren, Paul Waarts and Anna Ciapa are acknowledged for the discussions on the approach and the results.

Appendix. Distributions of the uncertainties in the stress ranges

This appendix provides the distributions of the multiplicative uncertainty factors on the stress range used in Eq. (9).

Variable M_{glob} describes the uncertainty in predicting the global (i.e. far field) stress using an engineering model. The distribution of M_{glob} is recommended as lognormal with a mean of 1.0 and a standard deviation of 0.1 in the JCSS probabilistic model code [43].

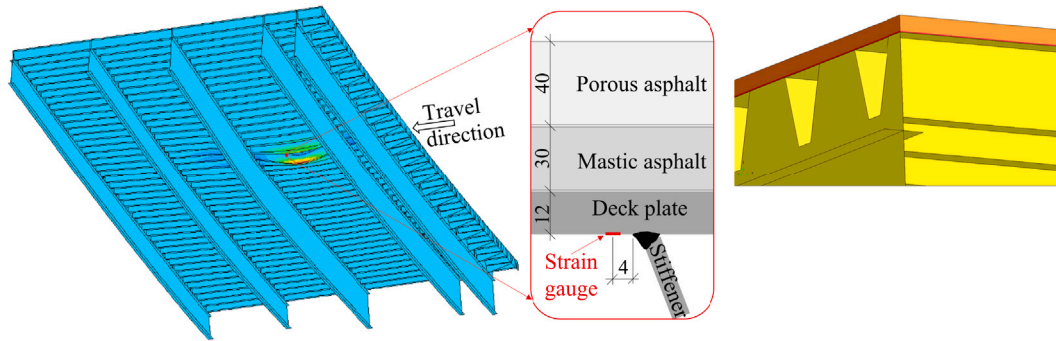


Fig. A.18. Engineering model of the OBD of the Van Brieneoord bridge with a load applied near the strain gauge position (dimensions in mm).

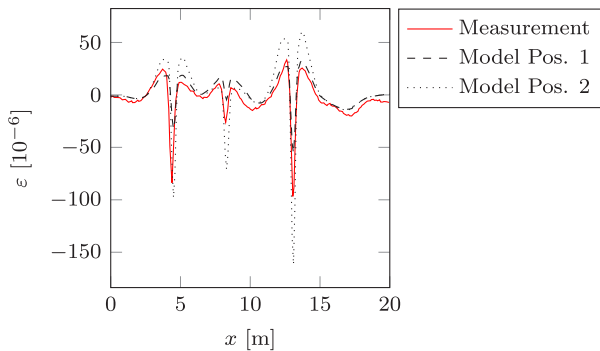


Fig. A.19. Examples of influence lines predicted by the model at two lateral positions and a measured influence line (80 km/h) in between these positions of the Van Brieneoord OBD.

This distribution, adopted here, is verified using engineering models and measurements on a number of bridges in [40].

The hot-spot stress or other local structural stress is not only commonly used for the verification of Detail 5, but also for other deck plate and stringer details, see [48–56] for Detail 1, [54,57–64] for Detail 2, [48,55,56,62,65–67] for Detail 3 and [53,65,68] for Detail 4. It is therefore important to consider a model uncertainty factor related to the calculation of the Stress Concentration Factor (SCF). The distribution of M_{scf} is recommended as lognormal with a mean of 1.0 and a standard deviation of 0.2 in [43]. This implies a large scatter in the evaluation of the SCF. The offshore guideline DNV-RP-C210 [69] recommends a normal distribution with a mean of 1.0 and a standard deviation of 0.05. Further study is done because of the large difference in the distribution between the two guidelines. A number of round-robin studies is given in literature where the SCF of the same structural detail is evaluated with the finite element model, using different element types, different engineers (or scholars) and different software. A hot-spot SCF was determined for a transverse welded attachment in [70], with a Coefficient of Variation (CoV) of 0.03 (over all mesh types, software and users). It was 0.08 for a different definition of the hot-spot SCF. The CoV was 0.04 for the SCF at a longitudinal attachment. Fricke et al. [71,72] evaluated more complex details (with higher SCFs) than those in [70]. The CoV of the SCF was 0.04, 0.03 and 0.09 for a doubler plate, an edge gusset and a stiffener on a T-bar, respectively (two details in [71] are excluded here because the evaluation of the hot-spot stress has changed in the meantime). The average CoV of the details in these studies is 0.05. As a comparison, the CoV of the effective notch stress computed in a similar way was 0.02 in [73].

The structures in sources [70–72] do not include OBDs. The strain close to Detail 5 is measured in a laboratory set-up in [31] and it agreed exactly with a prediction using a similar finite element model as the one

in Fig. 12. Additional data is subtracted from a measurement and model campaign of an OBD in practice, namely, the deck of the Van Brieneoord bridge. The campaign will be described elsewhere, but some results relevant for the current study are given here. Four strain gauges are attached to the bottom of the deck plate in transverse direction, close to the welds with the stiffeners, at quarter span distance between two crossbeams and 4.5 m away from the expansion joint. This gauge location is representative of the hot-spot strain of Detail 1 (Fig. 1). The strains are measured during the crossing of vehicles with known axle loads at different environmental temperatures. A finite element model is developed to predict the strains at the same locations. Different than the model of Fig. 12, the finite element model of the bridge deck is considered representative for engineering practice, with the steel parts modelled in shell elements and the two asphalt layers modelled with solids and non-compositely connected to the steel parts, see Fig. A.18. The temperature-dependent asphalt stiffness is taken from [9]. The crossbeams are clamped at their ends, which are at the connections with the box-shaped main girders in the actual bridge. Influence lines are determined for discrete transverse positions. Fig. A.19 gives an example of the predicted influence lines of strain ϵ in traffic direction (x) for two lateral positions, and a measurement with a lateral position in between, for an asphalt temperature exceeding 30°C. The maximum strain ranges of each measured crossing and each predicted lateral position are determined. Fig. A.20 displays the results for one of the strain gauges. The ratio between measured and calculated strain range for all strain gauges is on average 0.91 (i.e. a conservative estimation) and the standard deviation is 0.17. This standard deviation comprises the total model uncertainty. Considering that the standard deviation of M_{glob} is selected as 0.1, the remaining standard deviation of M_{scf} is equal to $\sqrt{0.17^2 - 0.1^2} = 0.14$. However, some of the difference between the measurement and the model is expected to be related to the measurement set-up, where it appeared difficult to determine the exact lateral position of the vehicle. In addition, the temperature of the asphalt layer, the temperature-dependent asphalt stiffness, the asphalt thickness and the composite working of the asphalt and the steel deck are uncertain and they may contribute to the scatter. A deck without or with thin pavement is not subject to such uncertainties. For such a deck, which is more sensitive to the tyre contact surface, it is expected that the mean of the combined model uncertainty is closer to 1 and its standard deviation is lower.

Insufficient information is available to evaluate the type of distribution for the model uncertainty in the SCF. Obviously, a lognormal distribution is more detrimental and requires higher safety factors as compared to a normal distribution. Further, the number of observations of the CoV of the SCF is limited to 7. For this reason a Student's T distribution is used for the logarithm of M_{scf} with a mean of 0, a CoV equal to the average of the data of 0.06, and a degree of freedom of 6. The reliability simulations in the main part of the paper are also carried out for a lognormal distribution of M_{scf} with a CoV of 0.05 and with a

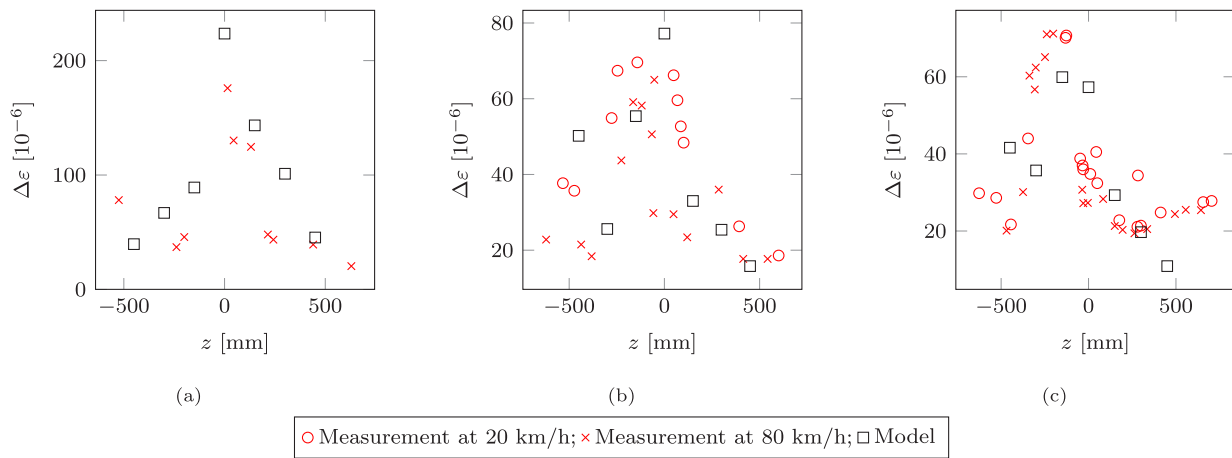


Fig. A.20. Maximum strain range versus lateral position predicted by the model and according to the measurements of the Van Brienoord OBD for a strain gauge attached to the deck plate: (a) During a summer day (asphalt temperature > 30 °C); (b) During a summer night (25 °C); (c) During a winter night (5 °C).

CoV of 1.0. The difference in partial safety factor γ_{F_f} to meet the target reliability is less than 0.05 with these two alternatives.

The data of Fig. A.20 allow to estimate the dynamic amplification factor as the ratio between the strains measured at low speed vehicle crossings (20 km/h) and at full speed crossings (80 km/h). The transverse deck plate strains are on average 2% lower at full speed compared to low speed. Strain gauges attached to the bottom of the stringers in the same campaign give a 0%–5% lower strain at full speed compared to low speed. Liu et al. [74] carried out a similar measurement campaign. The strains at full speed (60 km/h) were 1% higher, 8% lower and 13% lower than at low speed (5 km/h) for the stringer-to-crossbeam joint, the deck plate and the stringer bottom, respectively. A possible explanation for the reduction of strain at full speed is the strain rate dependency of the stiffness of the asphalt layer, which is not considered in engineering models and which would not apply in a deck without pavement. The Van Brienoord measurement campaign shows a scatter of approximately 10% between the different measurements. However, part of this scatter is attributed to the difficulty in determining the lateral position of the test vehicle. Moreover, the scatter implies that it varies per crossing whereas the formulation of Eq. (9) implies a dynamic amplification equal for all crossings. A low influence of the speed of heavy (i.e. fatigue-relevant) freight vehicles on the response was also observed for the superstructures of steel road bridges of various span in [40] and for concrete road bridges in [75]. The dynamic amplification factor M_{dyn} is modelled using a lognormal distribution with a mean of 1 and a standard deviation of 0.02. It should be noted that the pavement surface quality can have a significant influence on the dynamic amplification [76]. The distribution used here is valid for well maintained pavement.

Generally, it is assumed that axle loads increase in time. However, data are not available from which such a trend can be derived. The load models as based on the Auxerre WIM data from around 1985 are still conservative today [37], which could imply that the trend is small. On the other hand, electrification of lorries may imply higher axle loads in future. The trend factor M_{tr} used here is taken from [40], resulting in an approximate mean trend factor of 1.1 over the design life of 100 years. A coefficient of variation of this trend of 0.05 is assumed.

The WIM measurement system comes with a certain accuracy. The scatter in the load measurement has a limited influence on the fatigue damage, because an axle with a too high measured load is almost compensated by another axle with a too low measured load. Bias, however, is important. By comparing measured strains with simulations of strains, the latter determined with WIM axle loads and measured influence lines, it appeared that the accuracy of the WIM system is high [39]: the shapes of the measured and WIM-based strain spectra were closely aligned and the WIM-based strain ranges had to be altered

with a factor between 1 and 1.03 (bias) to obtain the same ranges as in the measurement. The load measurement uncertainty M_{uim} used here is normal distributed with a mean of 1 and a standard deviation of 0.03.

References

- [1] Bocchieri WJ, Fisher JW. Williamsburg Bridge replacement orthotropic deck as-built fatigue test. Tech. rep., Lehigh University; 1998.
- [2] Zhang QH, Bu YZ, Li Q. Review on fatigue problems of orthotropic steel bridge deck. China J Highw Transp 2017;30(3):14–30.
- [3] Wang P, Pei X, Dong P, Song S. Traction structural stress analysis of fatigue behaviors of rib-to-deck joints in orthotropic bridge deck. Int. J. Fatigue 2019;125:11–22.
- [4] Yang H, Wang P, Qian H, Dong P. Modeling of fatigue failure mode in U-rib to deck joints in orthotropic bridge structures. Fatigue Fract. Eng. Mater. Struct. 2022;45(9):2721–33.
- [5] EN1991-2 + C1. Eurocode 1: Actions on structure – part 2: Traffic loads on bridges. CEN; 2015.
- [6] Nieuwsma R. Inventory of wheel loading and tyre inflation pressure in practice – measurements within framework of COST-334. Tech. rep., European Commission; 1999.
- [7] Faber A, Hahn WD. Effects of wide single tyres and dual tyres—A technical and economic approach—report on cost 334. Eng Trans 2000;48(3):261–72.
- [8] Fernando EG, Musani D, Park D-W, Liu W. Evaluation of effects of tire size and inflation pressure on tire contact stresses and pavement response. No. FHWA/TX-06/0-4361-1. Tech. rep., Texas Transportation Institute; 2006.
- [9] De Jong F. Renovation techniques for fa-tigue cracked orthotropic steel bridge decks [Ph.D. thesis], Delft University of Technology; 2007.
- [10] Groenendijk J. Accelerated testing and surface cracking of asphaltic concrete pavements [Ph.D. thesis], Delft University of Technology; 1998.
- [11] Sebastian WM, Ralph M, Poulton M, Goacher J. Lab and field studies into effectiveness of flat steel plate–rubber pad systems as tyre substitutes for local loading of cellular GFRP bridge decking. Composites B 2017;125:100–22.
- [12] Wang R, Inman F, Machemehl R, Zhang Z, Walton CM. Study of current truck configurations. Tech. rep., Centre for Transportation Research; 2004.
- [13] De Beer M. Reconsideration of tyre-pavement input parameters for the structural design of flexible pavements. In: Proc. 10th int. conf. asphalt pavements. 2006, p. 13.
- [14] De Beer M, Maina JW, Rensburg Y, Greben JM. Toward using tire-road contact stresses in pavement design and analysis. Tire Sci Technol 2012;40:246–71.
- [15] De Beer M, Sadzik EM, Fisher C, Coetzee CH. Tyre-pavement contact stress patterns from the test tyres of the Gautrans heavy vehicle simulator (HVS) MK IV+. In: Proc. 24th South African transport conf.. 2005, p. 413–30.
- [16] De Beer M, Fisher C, Jooste FJ. Determination of pneumatic tyre/pavement interface contact stresses under moving loads and some effects on pavements with thin asphalt surfacing layers. In: Proc. 8th int. conf. asphalt pavements, vol. 1. International Society for Asphalt Pavements Lino Lakes, Minn.; 1997, p. 179–227.
- [17] De Beer M, Fisher C. Stress-in-motion (SIM) system for capturing tri-axial tyre–road interaction in the contact patch. Measurement 2013;46(7):2155–73.
- [18] Douglas RA, Woodward WD, Woodside A. Road contact stresses and forces under tires with low inflation pressure. Can. J. Civil Eng. 2000;27(6):1248–58.
- [19] Tielking JT, Roberts FL. Tire contact pressure and its effect on pavement strain. J. Transp. Eng. 1987;113(1):56–71.

- [20] (No names). ENV 1991-3 – traffic loads on bridges – background and notes for guidance. Tech. rep., European Commission; 1994.
- [21] Prat M, Jacob B. Local load effects on road bridges. In: Heavy vehicles and roads: technology, safety and policy: Proceedings of the third international symposium on heavy vehicle weights and dimensions. Thomas Telford Publishing; 1992, p. 156.
- [22] NN. AASHTO LRFD bridge design specifications. American association of state highway and transportation officials; 2012.
- [23] Hengeveld ST, Vervuurt A, Maljaars J. Evaluation of the contact area of lorry tyres in Eurocode's fatigue load model 4 (FLM4). In: IABSE congress, Ghent 2021: structural engineering for future societal needs. 2021, p. 1–8.
- [24] Ono S, Shimozato T, Inaba N, Miki C. Propagation behaviour of fatigue crack penetrating into steel deck plate at connection with transverse rib and trough rib – IIW document XIII-2070-05. Tech. rep., International Institute of Welding; 2005.
- [25] Kolstein MH. Fatigue classification of welded joints in orthotropic steel bridge decks [Ph.D. thesis], Delft University of Technology; 2007.
- [26] Uchida D, Mori T. Wheel running fatigue test for orthotropic steel bridge decks – IIW document XIII-2433-12. Tech. rep., International Institute of Welding; 2012.
- [27] Pijpers R, Pahlavan P, Paulissen J, et al. Structural health monitoring for fatigue life prediction of orthotropic bridge decks. In: Proc. 3rd orthotropic bridge conference. 2013, p. 432–445.
- [28] Konda N, Nishio M, Ichimiya M, Kasugai T, Kiyokawa S. Development of fatigue test method and improvement of fatigue life by new functional steel plates for welding of trough rib and deck plate of orthotropic decks. Int. J. Steel Struct. 2013;13(1):191–7.
- [29] Dung CV, Sasaki E, Tajima K, Suzuki T. Investigations on the effect of weld penetration on fatigue strength of rib-to-deck welded joints in orthotropic steel decks. Int. J. Steel Struct. 2015;15(2):299–310.
- [30] Chen Y, Lv P, Li D. Research on fatigue strength for weld structure details of deck with u-rib and diaphragm in orthotropic steel bridge deck. Metals 2019;9(5):484–99.
- [31] Maljaars J, Bonet E, Pijpers RJM. Fatigue resistance of the deck plate in steel orthotropic deck structures. Eng. Fract. Mech. 2018;201:214–28.
- [32] Maljaars J, van Dooren F, Kolstein MH. Fatigue assessment for deck plates in orthotropic bridge decks. Steel Constr. 2012;5(2):93–100.
- [33] EN1993-1-9 + C2. Eurocode 3: design of steel structures – part 1-9: fatigue. CEN; 2009.
- [34] BS7608. Guide to fatigue design and assessment of steel products. BSI; 2014.
- [35] Palmgren A. Die Lebensdauer von Kugellagern. Zeitschrift 1924;68:339–41.
- [36] Miner M. Cumulative damage in fatigue. Trans ASME J Appl Mech 1945;12:A159–64.
- [37] Croce P. Impact of road traffic tendency in Europe on fatigue assessment of bridges. Appl. Sci. 2020;10(4):1389.
- [38] NEN8701+A1. Assessment of existing structures in case of reconstruction and disapproval – actions (in Dutch). NEN; 2020.
- [39] Maljaars J. Evaluation of traffic load models for fatigue verification of European road bridges. Eng. Struct. 2020;225:111326.
- [40] Maljaars J, Leonetti D, Hashemi B, Snijder HH. Systematic derivation of safety factors for the fatigue design of steel bridges. Struct. Saf. 2022;97:102229.
- [41] Yang Z, Sebastian W. Nonlinear behaviour of pultruded decks due to morphing of tyre loads. Eng. Struct. 2023;274:115146.
- [42] Wirsching PH. Fatigue reliability for offshore structures. J. Struct. Eng. 1984;110(10):2340–56.
- [43] JCSS. JCSS probabilistic model code. Joint Committee of Structural Safety (JCSS); 2013, URL <https://www.jcss-lc.org/jcss-probabilistic-model-code/>.
- [44] prEN1993-1-9. Final document of Eurocode 3: design of steel structures – part 1-9: fatigue. CEN; 2022.
- [45] prEN1990. Enquiry document of Eurocode — Basis of structural and geotechnical design. CEN; 2022.
- [46] Baptista C, Reis A, Nussbaumer A. Probabilistic SN curves for constant and variable amplitude. Int. J. Fatigue 2017;101:312–27.
- [47] D'Angelo L, Nussbaumer A. Estimation of fatigue SN curves of welded joints using advanced probabilistic approach. Int. J. Fatigue 2017;97:98–113.
- [48] Bignonnet A, Jacob B, J. C., LaFrance M. Fatigue resistance of orthotropic steel decks. In: Proc. IABSE workshop, Lausanne. 1991, p. 227–36.
- [49] Yuan H. Optimization of rib-to-deck welds for steel orthotropic bridge decks [Ph.D. thesis], Virginia Tech; 2011.
- [50] Nagy W. Fatigue assessment of orthotropic steel decks based on fracture mechanics [Ph.D. thesis], Ghent University; 2017.
- [51] Cheng B, Ye X, Cao X, Mbako DD, Cao Y. Experimental study on fatigue failure of rib-to-deck welded connections in orthotropic steel bridge decks. Int. J. Fatigue 2017;103:157–67.
- [52] Heng J, Zheng K, Gou C, Zhang Y, Bao Y. Fatigue performance of rib-to-deck joints in orthotropic steel decks with thickened edge U-ribs. J. Bridge Eng. 2017;22(9):04017059.
- [53] Ocel JM, Cross B, Wright WJ, Yuan H, et al. Optimization of rib-to-deck welds for steel orthotropic bridge decks. Tech. rep., United States. Federal Highway Administration; 2017.
- [54] Kainuma S, Yang M, Jeong Y-S, Inokuchi S, Kawabata A, Uchida D. Experimental investigation for structural parameter effects on fatigue behavior of rib-to-deck welded joints in orthotropic steel decks. Eng. Fail. Anal. 2017;79:520–37.
- [55] Li M, Suzuki Y, Hashimoto K, Sugiura K. Experimental study on fatigue resistance of rib-to-deck joint in orthotropic steel bridge deck. J. Bridge Eng. 2018;23(2):04017128.
- [56] Li J, Zhang Q, Bao Y, Zhu J, Chen L, Bu Y. An equivalent structural stress-based fatigue evaluation framework for rib-to-deck welded joints in orthotropic steel deck. Eng. Struct. 2019;196:109304.
- [57] Maddox S. The fatigue behaviour of trapezoidal stiffener to deck plate welds in orthotropic bridge decks, Supplementary Report 96UC. Tech. rep., Transport and Road Research Laboratory; 1974.
- [58] Ya S, Yamada K, Ishikawa T. Fatigue evaluation of rib-to-deck welded joints of orthotropic steel bridge deck. J. Bridge Eng. 2011;16(4):492–9.
- [59] Fu Z, Ji B, Zhang C, Li D. Experimental study on the fatigue performance of roof and U-rib welds of orthotropic steel bridge decks. KSCE J Civ Eng 2018;22(1):270–8.
- [60] YuanZhou Z, Ji B, Li D, Fu Z. Fatigue strength and root-deck crack propagation for U-rib to deck welded joint in steel box girder. Int. J. Steel Struct. 2018;18(5):1589–97.
- [61] Luo P, Zhang Q, Bao Y, Bu Y. Fatigue performance of welded joint between thickened-edge U-rib and deck in orthotropic steel deck. Eng. Struct. 2019;181:699–710.
- [62] Luo P, Zhang Q, Bao Y. Rib loading effects on weld root fatigue failure modes at rib-to-deck welded joint. Fatigue Fract. Eng. Mater. Struct. 2020;43(7):1399–418.
- [63] Wang D, Xiang C, Ma Y, Chen A, Wang B. Experimental study on the root-deck fatigue crack on orthotropic steel decks. Mater. Des. 2021;203:109601.
- [64] Yang H, Wang P, Qian H, Niu S, Dong P. An experimental investigation into fatigue behaviors of single-and double-sided U rib welds in orthotropic bridge decks. Int. J. Fatigue 2022;159:106827.
- [65] Ya S. Fatigue durability evaluations of trough to deck plate welded details of orthotropic steel deck [Ph.D. thesis], Nagoya University; 2009.
- [66] Thonnard J, Janss J. Comportement en fatigue des dalles orthotropes avec raidisseurs trapezoidaux. Tech. rep., Centre de Recherches Scientifiques et Techniques de l'Industrie des Fabrications Metalliques; 1985.
- [67] Janss J. Fatigue of welds in orthotropic bridge deck panels with trapezoidal stiffeners. J. Construct. Steel Res. 1988;9(2):147–54.
- [68] Yang H, Wang P, Qian H, Dong P. Analysis of fatigue test conditions for reproducing weld toe cracking into U-rib wall in orthotropic bridge decks. Int. J. Fatigue 2022;162:106976.
- [69] DNV-RP-C210. Probabilistic methods for planning of inspection for fatigue cracks in offshore structures. Det Norske Veritas; 2019.
- [70] Nussbaumer A, Grigoriou V. Round robin on local stress evaluation for fatigue by various FEM software. In: 69th international institute for welding (IIW) annual assembly and international conference. 2016, p. IIW doc XIII-2650–16.
- [71] Fricke W. Recommended hot-spot analysis procedure for structural details of ships and FPSOs based on round-robin FE analyses. Int J Offshore Polar Eng 2002;12(01).
- [72] Fricke W, Kahl A. Comparison of different structural stress approaches for fatigue assessment of welded ship structures. Mar. Struct. 2005;18(7–8):473–88.
- [73] Fricke W. Round-robin study on stress analysis for the effective notch stress approach. Weld World 2007;51(3):68–79.
- [74] Liu XG, Zhao XX, Zhang YL. Research on static and dynamic tests of steel orthotropic decks. Appl. Mech. Mater. 2011;94:1291–7.
- [75] Kalin J, Žnidarič A, Anžlin A, Kreslin M. Measurements of bridge dynamic amplification factor using bridge weigh-in-motion data. Struct Infrastructure Eng 2022;18(8):1164–76.
- [76] Zhang W, Cai CS. Reliability-based dynamic amplification factor on stress ranges for fatigue design of existing bridges. J. Bridge Eng. 2013;18(6):538–52.